# Supplementary Information

# Giant odd-parity magnetoresistance from proximity-induced topological states

Tomoki Hotta[1], Le Duc Anh[1,2*], Takahiro Chiba[3,4], Yohei Kota[5], and Masaaki Tanaka[1,2,6*]

[1]*Department of Electrical Engineering and Information Systems, The University of Tokyo*

[2]*Center for Spintronics Research Network (CSRN), The University of Tokyo*

[3] *Department of Information Science and Technology, Graduate School of Science and Engineering, Yamagata University, Japan*

[4]*Department of Applied Physics, Graduate School of Engineering, Tohoku University*

[5]*National Institute of Technology, Fukushima College*

[6]*Institute for Nano Quantum Information Electronics (NanoQuine)*

## Supplementary Table and Figures

**Supplementary Table S1|** Comparison of the OMR values, defined as $[R(B) - R(-B)] / [2 \times R(0\ \mathrm{T})]$, reported so far.

| Material | Maximum OMR (%) | $B$ (T) | Reference |
|---|---|---|---|
| $Eu_2Ir_2O_7$ | 0.4% | 9 | [S1] |
| $SmCo_5$ | 0.05% | 0.5 | [S2] |
| InAs/(Ga,Fe)Sb | 13.5% | 10 | [S3] |
| bilayer graphene/$Cr_2Ge_2Te_6$ | 40% | 14 | [S4] |
| α-Sn/(In,Fe)Sb | **1150%** | **1** | **This work** |

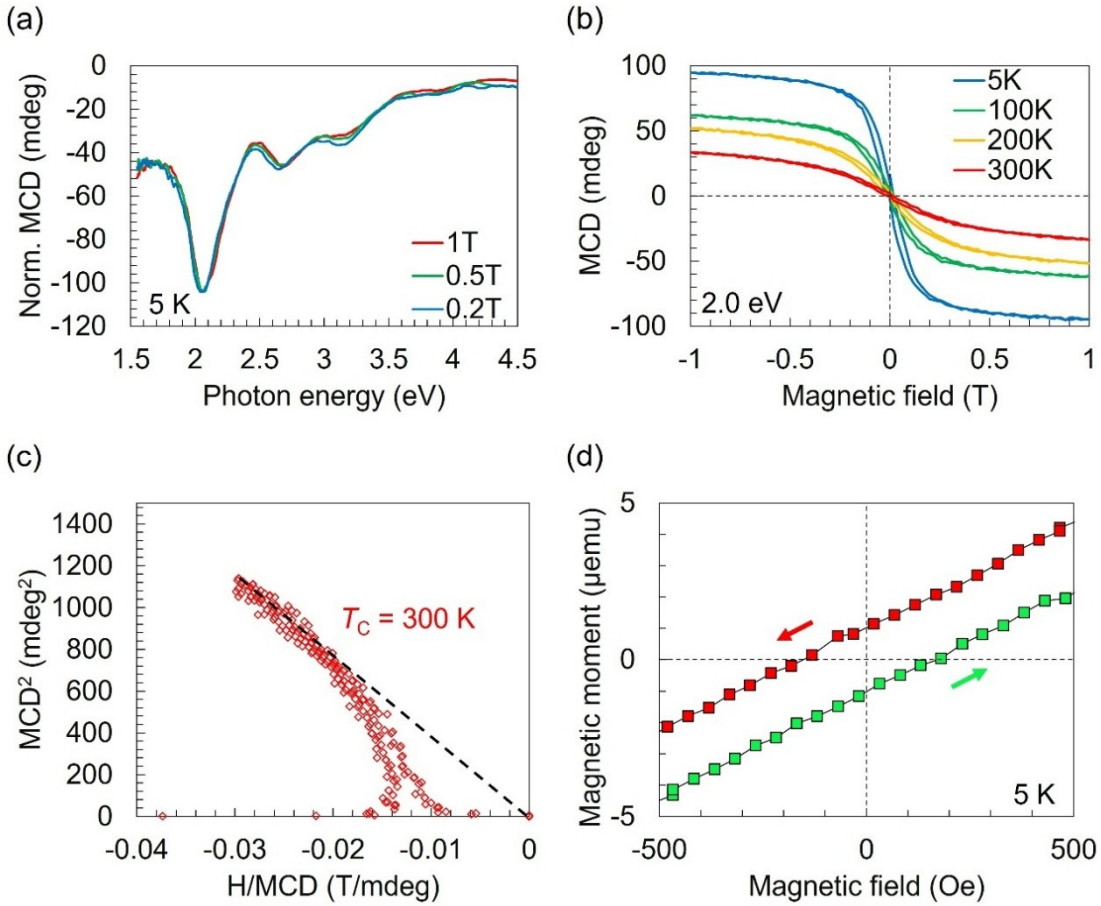


**Supplementary Fig. S1 | Magnetic properties of the (In,Fe)Sb layer.** (a) Reflection magnetic circular dichroism (MCD) spectra measured at 5 K under various perpendicular magnetic fields. MCD intensities at 0.5 T and 0.2 T are normalized to the spectrum at 1 T. (b) MCD intensity – magnetic field (*MCD* – *H*) curves measured at various temperatures. The MCD intensity was at taken at 2.0 eV. (c) Arrott plot derived from the *MCD* – *H* curve at 300 K, used to estimate the Curie temperature. (d) Magnetization – magnetic field (*M* – *H*) curve measured by SQUID magnetometry at 5 K.

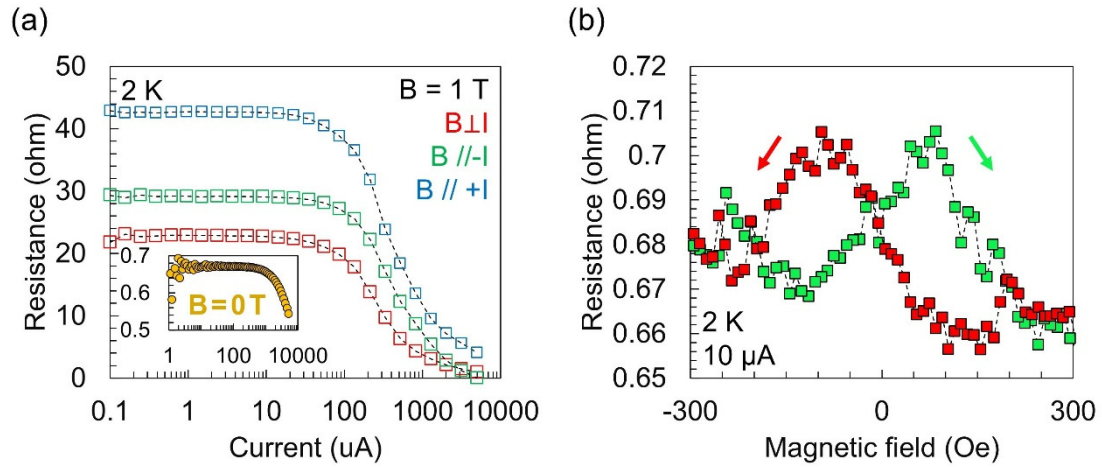


**Supplementary Fig. S2 | Current and magnetic field dependences of the longitudinal resistance at 2 K.** (a) Current dependence of the longitudinal resistance measured at 2 K. Red, green, and blue data points correspond to the measurements under a 1 T magnetic field applied perpendicular to the film plane (***B*** $\perp$***I***), oriented antiparallel (***B***//–***I***), and parallel (***B***//+***I***) to the current direction, respectively. The inset shows data (yellow points) taken under zero magnetic field. (b) Magnetic field dependence of the longitudinal resistance at 2 K under a perpendicular magnetic field. The peak positions (±100 Oe) correspond to the coercive field in the $M - H$ curve of Fig. S1(d).

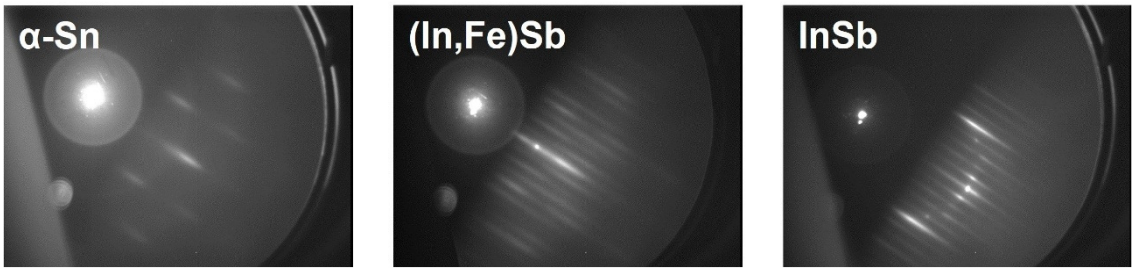


**Supplementary Fig. S3 |** RHEED pattern of each layer during the MBE growth along the [110] direction.

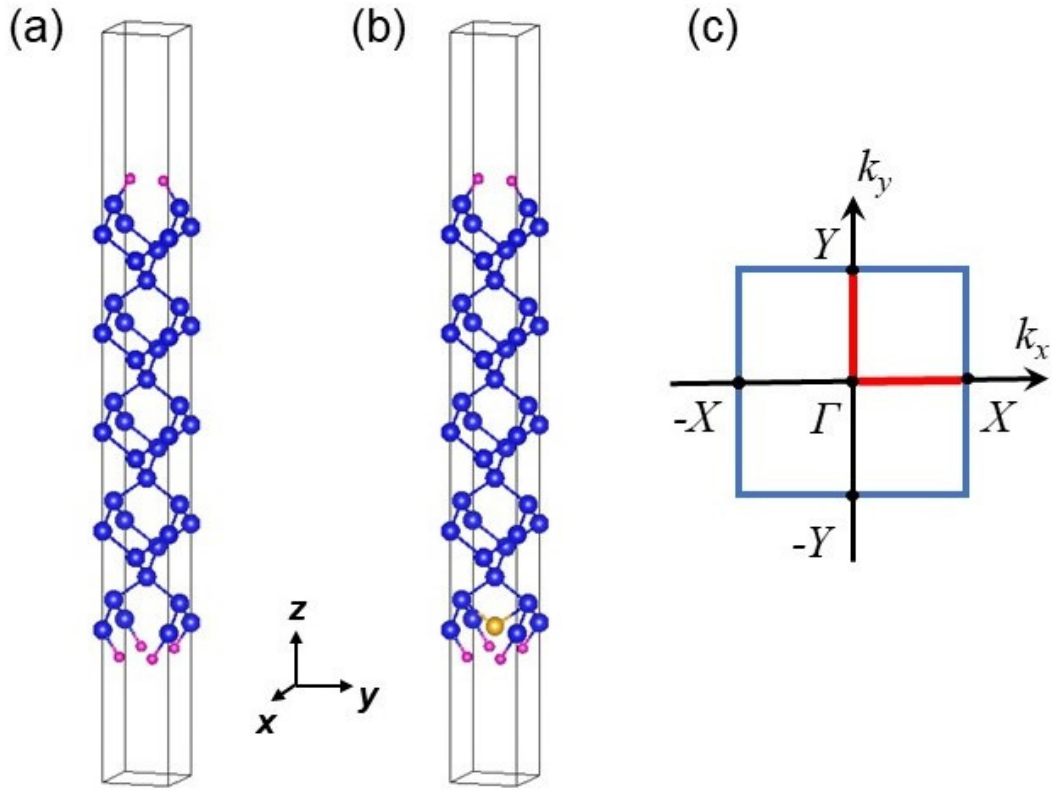


**Supplementary Fig. S4 | Crystal structures used in slab calculations.** (a) Slab geometry of α-Sn/vacuum. (b) Slab geometry of α-Sn/Fe along the [001] direction. Sn, Fe, and H atoms are represented by blue, yellow, and pink spheres, respectively. (c) Definition of the two-dimensional Brillouin zone in our calculation. Here, $X = (\pi/a^*,0)$ and $Y = (0, \pi/a^*)$ are on the Brillouin zone boundary in the $k_z = 0$ plane. $a^* = a/\sqrt{2}$ is the in-plane lattice constant of the tetragonal unit cell of α-Sn in our calculations, where $a$ is the lattice constant of the diamond-type unit cell of α-Sn.

## Supplementary note 1

We characterized the magnetic properties of our heterostructure sample using magnetic circular dichroism (MCD) spectroscopy and superconducting quantum interference device (SQUID) magnetometry. Supplementary Fig. S1(a) presents the MCD spectra measured at 5 K under magnetic fields of 1 T, 0.5 T, and 0.2 T, applied perpendicular to the film plane. The spectra obtained at 0.5 T and 0.2 T are normalized to that at 1 T. All the normalized spectra are almost perfectly overlapped, featuring a negative peak at 2.0 eV ($E_1$) and a positive peak at 2.5 eV ($E_1 + \Delta_1$)—a spectral signature characteristic of the intrinsic ferromagnetism in (In,Fe)Sb [S5]. The magnetic field dependence of the MCD intensity (*MCD–H* curves), measured at a photon energy of 2.0 eV [Supplementary Fig. S1(b)], shows clear ferromagnetic hysteresis. From the Arrott plot analysis[S6], the Curie temperature ($T_C$) is estimated to be 300 K [Supplementary Fig. S1(c)]. SQUID magnetometry at 5 K [Supplementary Fig. S1(d)] reveals a coercive field of approximately 100 Oe, further confirming the ferromagnetic nature of the (In,Fe)Sb layer.

## Supplementary note 2

Supplementary Figure S2(a) shows the current ($I$) dependence of the longitudinal resistance under a magnetic field of 1 T. For currents below 10 μA, the resistance remains constant, indicating stable conduction behavior. However, when the current exceeds 10 μA, the resistance decreases monotonically with increasing the current. This behavior is likely attributed to a change in the current distribution. At low current ($I$ < 10 μA), conduction predominantly occurs within the α-Sn layer due to its semi-metallic nature. It is worth noting that the (In,Fe)Sb layer is insulating at low temperatures because of carrier localization induced by Fe 3d states[S5]. The observed resistance decrease at higher currents ($I$ > 10 μA) may be due to current leakage into the underlying InSb buffer layer, possibly penetrating through the nominally insulating (In,Fe)Sb.

All the transport measurements in this study were performed at $I$ = 10 μA, ensuring that the current primarily flows through the α-Sn layer. Under this condition, we also observe clear hysteresis in the magnetoresistance at 2 K [Supplementary Fig. S2(b)], with peaks at ±100 Oe corresponding to the coercive field of approximately 100 Oe [Supplementary Fig. S1(d)]. This hysteresis indicates that the α-Sn layer becomes magnetized via the adjacent ferromagnetic (In,Fe)Sb layer. Such a phenomenon, where the magnetic order of one material influences an adjacent layer through quantum mechanical coupling, is known as the magnetic proximity effect.

## Supplementary note 3

Here, we comment on the validity of comparing the resistance and current in the context of our measurements and theoretical model. In the experiment, a constant direct current $I_{\mathrm{DC}}$ is applied, and the voltage change upon magnetic field reversal is detected as the OMR signal: $V_{\mathrm{odd}}^{\mathrm{exp.}} = R_{\mathrm{odd}}^{\mathrm{exp.}} \times I_{\mathrm{DC}}$. On the other hand, semiclassical transport theory—where the net current arises from a shift of a rigid Fermi surface—predicts a voltage signal proportional to the current density: $V_{\mathrm{odd}}^{\mathrm{calc.}} \propto j_{\mathrm{odd}}^{\mathrm{calc.}}$. Assuming that the experimentally observed voltage equals the theoretically calculated one, $V_{\mathrm{odd}}^{\mathrm{exp.}} = V_{\mathrm{odd}}^{\mathrm{calc.}}$, it follows that: $R_{\mathrm{odd}}^{\mathrm{exp.}} \propto j_{\mathrm{odd}}^{\mathrm{calc.}}$. This proportionality justifies the comparison between the experimentally measured OMR ratio and the theoretically calculated odd component of the current density.

## Supplementary note 4

For both the α-Sn/vacuum and α-Sn/Fe slab geometries, we used the layered tetragonal unit cell based on the diamond-type crystal structure deposited along the [001] direction, as shown in Supplementary Fig. S4. The 18 ML slab geometry was adopted for the computation of the topological surface state (TSS) of strained α-Sn. Both edges of the slab were terminated with H atoms to remove dangling bonds. On the other hand, for the computation of a strained α-Sn/Fe system, it was adopted that the 18 ML slab geometry in which a single Fe atom is embedded as a dopant on the lowest Sn layer. For both of the slab geometries, the surfaces were separated by a vacuum layer with a thickness of 20 Å. To calculate the strain effect on the topological electronic states, we considered a biaxial in-plane compressive strain of –0.76%[S7]. Fixing the in-plane lattice constant, structural optimization of atomic position was performed.

## Supplementary References


[S1]. Fujita, T. C., Kozuka, Y., Uchida, M., Tsukazaki, A., Arima, T., and Kawasaki, M., “Odd parity magnetoresistance in pyrochlore iridate thin films with broken time-reversal symmetry”, Sci. Rep. **5**, 9711 (2015).

[S2]. Wang, Y., Lee, P. A., Silevitch, D., Gomez, F., Cooper, S., Ren, Y., Yan,J.-Q., Mandrus, D., Rosenbaum, T. and Feng, Y., “Antisymmetric linear magnetoresistance and the planar Hall effect” Nature Commun. **11**, 216 (2020).

[S3]. Takiguchi, K., Anh, L. D., Chiba, T., Shiratani, H., Fukuzawa, R., Takahashi, T., and Tanaka, M., “Giant gate-controlled odd-parity magnetoresistance in one-dimensional channels with a magnetic proximity effect”, Nature Commun.**13**, 6538

(2022).

[S4]. Sahani, D., Das, S., Watanabe, K., Taniguchi, T., Agarwal, A. and Bid, A., “Giant gate-controlled room temperature odd-parity magnetoresistance in magnetized bilayer graphene”, Phys. Rev. Lett. **134**, 106301 (2025).

[S5]. Tu, N. T., Hai, P. N., Anh, L. D. and Tanaka, M., “High-temperature ferromagnetism in new n-type Fe-doped ferromagnetic semiconductor (In,Fe)Sb”, Appl. Phys. Express **11**, 063005 (2018).

[S6]. Arrott, A., “Criterion for Ferromagnetism from Observation of Magnetic Isotherms”, Phys. Rev. **108**, 1394 (1957).

[S7]. Anh, L. D., Takase, K., Chiba, T., Kota, Y., Takiguchi, K., and Tanaka, M., “Elemental Topological Dirac Semimetal α-Sn with High Quantum Mobility”, Adv. Mater. **33**, 2104645 (2021).